

The Observed Structure and Precipitation Characteristics of Southeast Atlantic Stratocumulus from Airborne Radar during ORACLES 2016–17

ANDREW M. DZAMBO AND TRISTAN L'ECUYER

University of Wisconsin–Madison, Madison, Wisconsin

OUSMANE O. SY AND SIMONE TANELLI

Jet Propulsion Laboratory, California Institute of Technology, Pasadena, California

(Manuscript received 6 February 2019, in final form 13 August 2019)

ABSTRACT

During the Observations of Aerosols above Clouds and Their Interactions (ORACLES) 2016 and 2017 field experiments, the Third Generation Advanced Precipitation and Cloud Radar (APR-3) flew aboard the NASA P-3 aircraft taking over 10 million profiles of stratocumulus clouds in the southeast Atlantic Ocean. This study documents cloud structure, precipitation frequency and intensity, and atmospheric stability for each flight during both field experiments. A larger cloud fraction was estimated for 2016, likely due to a larger estimated inversion strength (EIS) in the experiment area (between 6 and 10 K) compared to 2017 where EIS was on average 4–6 K lower. We used an optimal estimation retrieval to derive precipitation rates for all measurable clouds during both experiments. Over 30% of clouds observed during the 2016 experiment exhibited precipitation reaching the surface, but retrieved drizzle rates were below 0.01 mm h^{-1} in all but 40% of these profiles. This is in sharp contrast to the 2017 campaign where over 53% of precipitating profiles had rainfall rates larger than 0.01 mm h^{-1} . The differences in cloud and rain fractions between the two years are most likely due to differences in the sampling environments; however, enough variations in cloud, virga, and rain fraction exist for similar environmental conditions such that additional analysis of cloud and aerosol interactions—specifically their effect on precipitation processes—needs further exploration. The extensive APR-3 sampling of drizzling stratocumulus under similar thermodynamic conditions provides a rich dataset for examining the influence of biomass burning aerosols on cloud fraction, morphology, and precipitation characteristics in this climatically important region.

1. Introduction

Stratocumulus clouds (StCu) are the dominant cloud cover type over the world's oceans (Warren et al. 2007) and have a pronounced influence on Earth's energy balance (e.g., Wood 2012). Stratocumulus cloud properties, formation, and maintenance depend on a number of complex processes including entrainment between the planetary boundary layer (PBL) and free atmosphere (Gerber 1996), cloud condensation nuclei (CCN) concentration (Zhang et al. 2004), regional large-scale dynamics (Wood et al. 2002), and warm cloud microphysical processes such as condensation and collision-coalescence (Bennartz 2007). Precipitation processes affect StCu lifetime in a number of ways such as, for example, modulating number concentration (Mohrmann

et al. 2018) and scavenging CCN from the PBL (Albrecht 1989; Wood 2006). If a CCN can be activated and grow via coalescence to a sufficiently large size, drizzle can "wash out" aerosol particulates and other CCN from the PBL toward the ocean surface (Wood 2006) or, if the drizzle drop evaporates before reaching the ocean surface, the number of available CCN is still depleted from the cloud layer but redistributed through the PBL (Diamond et al. 2018). Precipitation processes are further complicated by environmental processes in which StCu reside and depend on local stability, relative humidity, liquid water path (LWP), and boundary layer decoupling (Wood 2012; Wood et al. 2018; Xue et al. 2008). Unsurprisingly, the diurnal variability of these processes and environmental variables adds yet another layer of complexity toward understanding precipitation processes in StCu clouds (Wood et al. 2002).

The representation of these processes in global climate models has proven challenging. Several studies

Corresponding author: Andrew M. Dzambo, adzambo@wisc.edu

have found that warm clouds precipitate too frequently and too often (Stephens et al. 2010; Trenberth 2011; Kay et al. 2018). It has been suggested that this could be due to a misrepresentation of precipitation efficiency for a given liquid water path (Jing et al. 2017). Precipitating StCu clouds could also act as a pathway toward cleansing the PBL of aerosol and, if the StCu deck is primarily open-cell (i.e., forming in less stable environments) as opposed to closed-cell (i.e., typically forming in regions of strong subsidence), these precipitating cells could suppress new cloud formation later in a diurnal cycle due to significant aerosol depletion (Wang et al. 2010). It is clear that precipitation processes play a role in StCu cloud morphology and lifetime, yet deconvolving these processes from aerosol effects and resultant radiative effects remains open for scientific debate (Stevens and Feingold 2009).

Ideally, studies focused on cloud–aerosol–precipitation processes would take place in the northeast Pacific Ocean, southeast Pacific Ocean, and southeast (SE) Atlantic Ocean, where stratocumulus clouds are commonly observed. In the SE Atlantic Ocean, the presence of a Southern Hemisphere wintertime biomass-burning (BB) layer over this region's StCu deck complicates cloud evolution and associated precipitation processes. Uncertainties in aerosol properties (Meyer et al. 2015; Peers et al. 2016; Sayer et al. 2016), radiative effects (Matus et al. 2015), and cloud morphology responses to these aerosols (Yamaguchi et al. 2015) have made the SE Atlantic Ocean among the most challenging regions of the globe to model (Zuidema et al. 2016).

StCu clouds, particularly those observed in the SE Atlantic, are usually homogeneous but challenging to observe for a number of reasons. Passive radiometers such as the Moderate Resolution Imaging Spectroradiometer (MODIS) or Geostationary Operational Environmental Satellite (GOES) can accurately measure cloud fraction and other macrophysical properties, yet they require numerous assumptions for precipitation rate retrievals that remain biased (Stenz et al. 2016). Multilayered clouds, cloud inhomogeneity, and overlying aerosol are all obstacles that complicate StCu cloud and precipitation observations. Precipitation rate products utilizing satellite microwave and infrared data have improved (Salio et al. 2015), but the precipitation retrieval quality is regime dependent (e.g., Berg et al. 2006) and these products do not provide the sensitivity to drizzle and rain required to study precipitation and microphysical processes (e.g., Berg et al. 2010).

W-band radar measurements from *CloudSat* (Tanelli et al. 2008), with a sensitivity of -29 dBZ , have improved our understanding of StCu clouds and warm rain processes (Lebsack et al. 2008; Haynes et al. 2009;

L'Ecuyer et al. 2009; Sorooshian et al. 2009; Lebsack and L'Ecuyer 2011). However, *CloudSat*'s “blind zone” below $\sim 750\text{ m}$ and its 240 m range resolution introduce limitations in the SE Atlantic where clouds can be much thinner than 240 m in depth and have cloud-top altitudes below 1 km . In such regimes, airborne remote sensing and in situ observations remain essential for process studies and validating satellite climatologies, especially over the remote ocean regions where ground-based validation studies are not possible.

A number of field experiments have gathered high-resolution cloud and boundary layer data in clouds across many major tropical and subtropical oceanic basins. The First ISCCP Regional Experiment (FIRE) campaign was among the earliest to collect observations of both cirrus and marine stratocumulus cloud systems, these observational datasets were used to characterize and validate cloud properties (Cox et al. 1987). The Dynamics and Chemistry of the Marine Stratocumulus (DYCOMS) experiments (Lenschow et al. 1988; Stevens et al. 2003) brought new insights on marine stratocumulus life cycle in the east Pacific Ocean near California, while also studying how atmospheric ozone interacts with these clouds. These early studies provided an important framework for future airborne-based validation studies of cloud and/or aerosol studies.

The Rain in Shallow Cumulus over the Ocean (RICO) experiment (Rauber et al. 2007) provided one of the most comprehensive datasets on warm rain processes. The continuous ground and ship-based measurements, combined with measurements from 57 research flights, have aided in the validation of cloud processes and cloud fraction (vanZanten et al. 2011) as well as sensitivity to rain microphysics (Abel and Shipway 2007) in large-eddy model simulations. In 2008, results utilizing data from the VAMOS Ocean-Cloud-Atmosphere-Land (VOCALS) improved our understanding of the land-ocean-atmosphere system (Wood et al. 2011; Bretherton et al. 2010). Data from VOCALS, at that time, was among the most robust to use for studying how cloud and precipitation processes in affect regional climate in the southeast Pacific. The Atlantic Stratocumulus Transition Experiment (ASTEX; Albrecht et al. 1995) and the Clouds, Aerosol, and Precipitation in the Marine Boundary Layer (CAP-MBL; Wood et al. 2015) focused on StCu in the northeast Atlantic. Recently, the Cloud System Evolution in the Trades (CSET) experiment utilized the high-performance instrumented airborne platform for environmental research (HIAPER) Cloud Radar and High Spectral Resolution lidar, complimented with a variety of in situ measurements, to study clouds in ultraclean boundary layers over the northeast Pacific Ocean (Albrecht et al. 2019). Until recently, however,

all such experiments have sampled clouds in the northeast Pacific, southeast Pacific, west Pacific, and northeast Atlantic. In these regions, StCu cloud decks are not influenced by a seasonal biomass-burning layer such as the one in the southeast Atlantic.

The Observations of Aerosols above Clouds and Their Interactions (ORACLES) campaign, taking place over the southeast Atlantic Ocean from 2016 to 2018, has provided new and unique observations for assessing cloud and aerosol interactions. Over the course of the first two years of the experiment, 18 different instruments have flown on the NASA ER-2 and P-3 aircrafts documenting aerosols, clouds, and precipitation and their interactions. The observational domain was extensive: measurements were collected from São Tomé ($\sim 0.2^{\circ}\text{N}$) to approximately 25°S and from Ascension Island to the western African coast. Among these instruments, the Third Generation Advanced Precipitation Radar (APR-3) measured profiles of collocated Ku- (13 GHz), Ka- (35 GHz), and W- (95 GHz) band reflectivity and Doppler velocity revealing cloud vertical structure and in-cloud precipitation processes in unprecedented detail. Over the course of the ORACLES 2016 and 2017 campaigns, the APR-3 collected over 10 million reflectivity profiles with vertical resolutions ranging from 35 to 8.6 m. Surface noise or “ground clutter” is limited to about 200 m (sometimes less) in the W-band observations enabling the study of near-surface precipitation (see sections 2 and 3 for more information).

We utilize the APR-3 radar data (with emphasis on the W band) and an adapted optimal estimation technique to estimate precipitation probability and rate, cloud fraction, and cloud-top height of StCu over the SE Atlantic Ocean during both the ORACLES 2016 and 2017 deployments. This paper utilizes this new APR-3 W-band precipitation dataset to document the characteristics of warm rain in two broad domains over the SE Atlantic observed during ORACLES 2016 and 2017. A preliminary analysis of the observed precipitation characteristics, supplemented with the European Centre for Medium-Range Weather Forecasts (ECMWF) interim reanalysis dataset (ERA-I; Dee et al. 2011), emphasizes the strong meteorological controls on cloud cover and warm rain in the SE Atlantic, reinforcing the need to account for such controls when addressing the aerosol–cloud–precipitation interactions objectives targeted by ORACLES.

2. The APR-3 dataset

The ORACLES experiment is the second field campaign to offer triple-frequency, simultaneously collocated

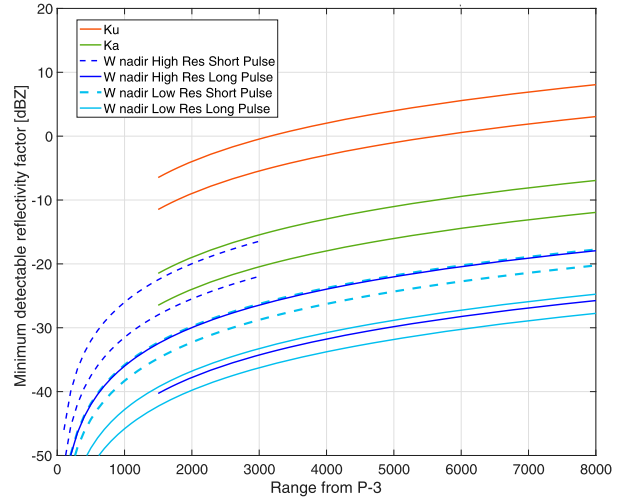


FIG. 1. Sensitivity of the Ku-, Ka-, and W-band channels as a function of distance from the aircraft for the ORACLES 2016 mission. The radar performance in 2017 was slightly improved due to upgrades in the processing system. Each set of lines represents a sensitivity range, which varied depending on the configuration of each scan.

radar data from the APR-3. The APR-3 was first deployed in the Olympic Mountains Field Experiment (OLYMPEx) in 2015 to study cold-cloud precipitation processes (Houze et al. 2017). During ORACLES 2016, over 3 million reflectivity profiles at each frequency were collected primarily in very stable, non- or lightly precipitating regions off the coast of Namibia while close to 7 million were sampled in 2017 in less stable, more inhomogeneous clouds with both convective and stratiform warm rain south of São Tomé. We emphasize W-band reflectivity measurements for this study due to their high sensitivity and ability to detect very thin StCu clouds (see Fig. 1). In this cloud regime, the utility of the Ku-band channel lies primarily in its measurements of ocean backscatter (a standard for radar calibration). The Ka-band channel role is primarily to provide an additional constraint for retrievals of light precipitation, and as transfer of the calibration reference from Ku to W band (through the comparison of observed reflectivity in regions where the Rayleigh assumption holds for a pair of radar bands). During high-altitude flight legs (typically around 6 to 7 km above ground level), the APR-3 W-band measurements were acquired with a long pulse ($1\ \mu\text{s}$), whereas for flight legs taking place directly above the StCu cloud deck (typically 100 to 300 m above the cloud top), a shorter pulse was sometimes adopted (typically 500 ns) since the sensitivity is greatly improved by the relatively short range. Furthermore, two products are routinely generated: a low-horizontal-resolution product (where pulses

are integrated for approximately 1 s, resulting in an along-track resolution of more than 100 m, depending on the aircraft ground speed) and a high-horizontal-resolution product (where integration spans only approximately 50 ms and the horizontal resolution is therefore mainly determined by the 0.9° antenna beamwidth, though this comes at the expense of about 10 dB in sensitivity due to the reduction in available independent samples in the process of noise estimation and subtraction). For comparison, the W-band high-resolution short pulses have sensitivity between -26 and -32 dBZ at 1 km away from the radar, while the long pulses have sensitivity between -35 and -38 dBZ at the same distance away from the aircraft. Overall, more than 10 million W-band radar profiles are available for 2016 and 2017, and additional W-band radar observations will be available from ORACLES once the 2018 dataset is processed, quality controlled and distributed.

A triple frequency radar scan from the 4 September 2016 research flight is shown in Fig. 2. StCu clouds are evident throughout this scan, and a pronounced shallow convective cell occurred between 21 and 28 km along this flight leg and is clearly evident in the Ka-band and W-band radar scans. The cloud-top height of this convective cell is approximately 1.4 km altitude in the W-band channel and below 1.3 km in the Ka-band channel demonstrating the enhanced sensitivity of the W-band radar to small liquid droplets near cloud top. Figure 2 also illustrates attenuation in the W-band channel: at 26 km, reflectivities between -2 and 0 dBZ are between 3 and 6 dBZ in the Ka-band channel (between 0.5 and 1.0 km). The surface backscatter or σ_0 data (overlaid on the top panel of Fig. 2) corroborate this by showing path-integrated attenuation (PIA) of 3–4 dB in this convective cell.

Surface clutter and background noise are removed from every W-band radar scene. Surface clutter in the APR-3 W-band dataset is typically present in the lowest six range bins (i.e., ~ 210 m above the surface). To avoid misinterpreting clutter as clouds or precipitation we mask all radar pixels below 200 m and compute an effective “surface” precipitation rate at this altitude. Background noise is first identified and removed following Marchand et al. (2008), which assigns values based on the likelihood of a radar return being a cloud. We remove background noise (certain cloud is assigned 40, etc.). This procedure eliminates most ground clutter and excludes surface returns, however, an extra step must be taken to eliminate noise that passed this initial screening. We removed remaining background noise by iteratively searching a 7×7 bin square and establishing the number of reflectivity values exceeding the minimum sensitivity at that range (see Fig. 1). If at least half of the reflectivity values in the 7×7 search square

are valid the data are kept in this scene otherwise the pixel is considered noise and all reflectivities in the box are masked. This methodology for removing background noise, adapted from Clothiaux et al. (1995) and Marchand et al. (2008), provides a compromise between removing obvious noise in the data without inadvertently removing legitimate cloud scenes, although some very thin, isolated cloud scenes may be screened. Removing noise and ground clutter in these scenes helps us more accurately quantify W-band-detected cloud-top and cloud-base heights improving our confidence in the resulting mean cloud-top and echo-base statistics while also providing unambiguous estimates of precipitation intensity.

3. Methods

Precipitation in StCu clouds is retrieved using an adapted version of the *CloudSat* 2C-RAIN-PROFILE (2C-RP) algorithm that has been adapted to airborne W-band radar observations (L'Ecuyer and Stephens 2002; Haynes et al. 2009; Mitrescu et al. 2010; Lebsack and L'Ecuyer 2011). 2C-RP was developed for *CloudSat* as a means to retrieve rainfall from space using a constrained iterative estimation technique. 2C-RP combines a reflectivity profile of any depth, a surface backscatter measurement (i.e., σ_0 or σ_0), a profile of gas attenuation derived from background atmospheric state variables, and surface state variables to retrieve profiles of size distribution parameters and associated liquid water contents and surface rainfall rates (Table 1). Cloud structure and retrieved rainfall rates are described in the context of estimated inversion strength (EIS, described in section 3d) in sections 4 and 5. The dataset generated by this adapted algorithm can be found online (Lebsack 2011), and Table 2 describes the variables in this dataset.

a. Gas attenuation correction

Airborne and spaceborne high-frequency radar measurements are susceptible to attenuation from water vapor. In the tropical oceans, W-band reflectivity can be attenuated as much as 2–4 dB (sometimes more). To account for this, APR-3 W-band reflectivity profiles are corrected for gas attenuation following Matrosov et al. (2004). We use profiles of temperature, specific humidity and total column water vapor from the ERA-I dataset (Dee et al. 2011) to derive appropriate gas attenuation profiles from both oxygen and water vapor.

b. Adapted 2C-PRECIP-COLUMN overview

Rainfall and drizzle are identified using an adapted version of *CloudSat*'s 2C-PRECIP-COLUMN algorithm (2C-PC; Haynes et al. 2009). Reflectivity profiles are tagged as rain possible, rain probable, or rain certain if

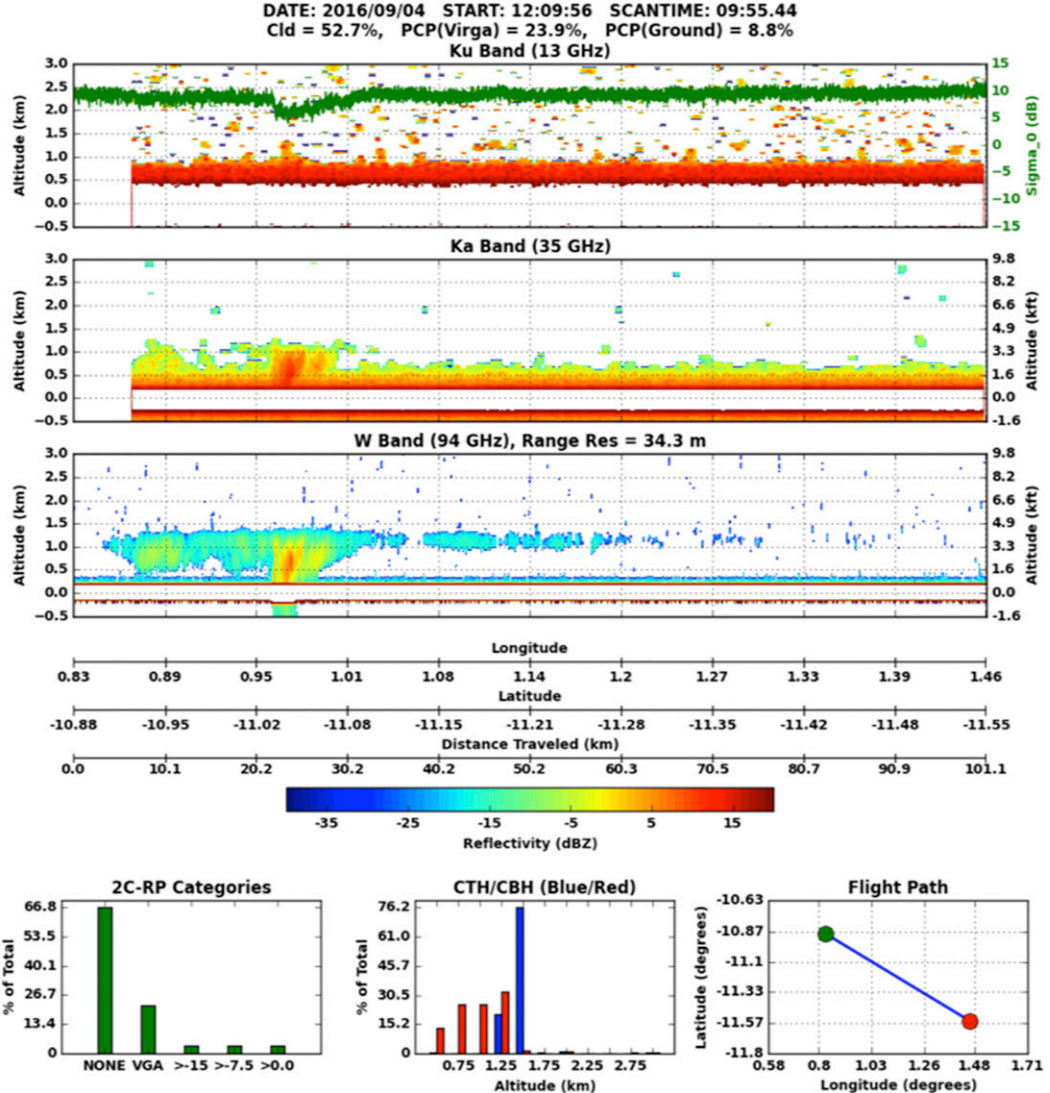


FIG. 2. APR-3 (top) Ku-band, (middle) Ka-band, and (bottom) W-band reflectivity image from 4 Sep 2016. This transect began at 1209:53 UTC and lasted for 9 min and 55 s. Latitude, longitude, and ground distance traveled are all shown as separate x axes. The color bar for reflectivity is tuned to W band (-40 to 20 dBZ) and is the same for all three radar images. Surface backscatter observed at W band (σ_0) is overlaid on the Ku-band image as a green line. The bottom-left histogram represents categories based on the 2C-PRECIP-COLUMN algorithm and shows (far left) clear-sky/thin cloud, (left) virga (percent of cloudy profiles with > -15 dBZ NOT reaching the surface), (middle) rain possible (surface reflectivity between -15 and -7.5 dBZ), (right) rain probable (surface reflectivity between -7.5 and 0 dBZ), and (far right) rain certain (surface reflectivity greater than 0 dBZ). The bottom-middle histogram shows the percentage of altitudes where cloud-base and cloud-top altitude occur (for all cloudy profiles in this scene). The bottom-right plot shows the flight track for this particular leg.

near-surface (200 m) reflectivities exceed -15 , -7.5 , and 0.0 dBZ, respectively. These categories can be loosely interpreted as light drizzle, drizzle, and rain though it should be noted that these terms correspond to precise reflectivity thresholds in subsequent discussion. An initial rain-rate intensity estimate and uncertainty is derived for all reflectivity profiles that contain drizzle or rain using the PIA and assuming a Marshall–Palmer drop size

distribution (Marshall and Palmer 1948). PIA is estimated by subtracting the W-band-observed σ_0 from a climatological clear-sky σ_0 , which is determined from a lookup table constructed by matching *CloudSat* clear-sky data to Advanced Microwave Sounding Radiometer (AMSR-E) sea surface temperature and wind speed observations for a wide range of scenes (Tanelli et al. 2008). The retrieved rainfall rate and PIA are used as the initial

TABLE 1. A list of variables required to run the adapted 2C-RAIN-PROFILE algorithm for ORACLES APR-3 data.

Variable	Data source or algorithm	Units	Data type/comments
W-Band reflectivity	APR-3	dBZ	Profile
Surface backscatter (σ_0)	APR-3	dBZ	Point measurement
Temperature	ERA-I	kelvin	Profile
Specific humidity	ERA-I	kg kg^{-1}	Profile
Altitude	ERA-I	meters	Profile; derived from ERA-I pressure using $p = p_0 e^{-z/H}$
Cloud mask	—	unitless	Estimated from reflectivity profile following the <i>CloudSat</i> classification criteria
Gas attenuation	ERA-I	dB	Estimated from ERA-I data following Matrosov et al. (2004)
Rain-rate estimate	2C-PRECIP-COLUMN	mm h^{-1}	Estimated from the adapted 2C-PRECIP-COLUMN algorithm
Rain-rate uncertainty	2C-PRECIP-COLUMN	%	Estimated from the adapted 2C-PRECIP-COLUMN algorithm

guess rainfall rate and an integral constraint, respectively, in 2C-RP.

c. 2C-RP algorithm description

Precipitation rate and liquid water content throughout the column are retrieved using an optimal estimation technique used to derive the *CloudSat* 2C-RP product ([Mitrescu et al. 2010](#); [Lebsock and L'Ecuyer 2011](#)). The adapted algorithm seeks to minimize the cost function

$$\Phi = [Z_{\text{sim}} - Z]^T \mathbf{S}_Z [Z_{\text{sim}} - Z] + [x - x_a]^T \mathbf{S}_a [x - x_a] + \frac{(\text{PIA}_{\text{sim}} - \text{PIA})^2}{\sigma_{\text{PIA}}^2},$$

where Z_{sim} and PIA_{sim} are the simulated reflectivity profile and simulated path-integrated attenuation (determined using a multiple-scattering model, described later in this

section), Z is the observed reflectivity profile, x_a is an a priori estimate of the background state, \mathbf{S}_z is the observational error covariance matrix, \mathbf{S}_a is the a priori error covariance matrix, and σ_{PIA} is the uncertainty in the PIA estimate. This cost function is minimized through Newtonian iteration to derive the precipitation rate estimate that matches the observations given the a priori and PIA constraints as well as their characteristics. Further details on the retrieval framework are covered extensively in [Lebsock and L'Ecuyer \(2011\)](#).

Simulated reflectivities are generated by assuming Mie scattering (for W-band reflectivity) to an assumed drop size distribution (DSD), where reflectivity is related to liquid water content (LWC) and precipitation rate. We assume a DSD following [Abel and Boutle \(2012\)](#). The [Abel and Boutle \(2012\)](#) DSD is represented by an exponential function; and, when compared to other

TABLE 2. List of variables in the Level 2 precipitation retrieval dataset.

Full name	Units	Dimensions	Comments/information
Precipitation flag	unitless	(time)	Precipitation occurrence flag
Quality flag	unitless	(time)	Precipitation quality flag (0 = no confidence, 4 = high confidence)
Status flag	unitless	(time)	Algorithm status (0 = computed from 2C-RP, 1 = passed through from 2C-PC)
Surface rain rate	mm h^{-1}	(time)	Surface rainfall rate, see text for data quality requirements
Surface rain-rate uncertainty	%	(time)	Uncertainty in the retrieved surface rainfall rate
Path-integrated attenuation	dB	(time)	Path-integrated attenuation estimated from 2C-RP
Liquid water path	g m^{-2}	(time)	Liquid water path through the depth of the cloud
Evaporation	kg kg^{-1}	(time)	Modeled evaporation from cloud base to surface based on Feingold (1993)
Attenuation-corrected reflectivity	dBZ	(time, height)	W-band reflectivity corrected for hydrometeor attenuation and multiple scattering
Hydrometeor attenuation	dB	(time, height)	Profile of hydrometeor attenuation computed by 2C-RP
Liquid water content	g m^{-3}	(time, height)	Profile of liquid water content estimated by 2C-RP using the AB13 DSD
Rain-rate profile	mm h^{-1}	(time, height)	Profile of rainfall rate estimated from liquid water content

DSD parameterizations, results in more realistic rainfall rates typically observed in StCu clouds. We acknowledge that, given the high vertical resolution of this data, considerable DSD variability will exist in individual profiles. Though we do not address the sensitivity of this method to the assumed DSD in this study, the availability of multiple collocated radar frequencies will make the direct retrieval of DSDs possible and will be the topic of future studies. Unlike approaches that utilize $Z-R$ relationships, 2C-RP accounts for non-Rayleigh scattering, models multiple scattering, and mitigates nonuniqueness caused by strong attenuation at W band through the a priori and PIA terms (L'Ecuyer and Stephens 2002).

It is possible for W-band radar observations to be entirely attenuated in heavy rainfall, but this generally only occurs when the precipitation rate exceeds 5 mm h^{-1} (Battaglia and Simmer 2008). These conditions rarely occurred during the ORACLES field deployment but were observed frequently in trade cumulus on the transit flights and in cumulus observed near the equator during ORACLES 2017. Multiple scattering (MS) is modeled following Hogan and Battaglia (2008). Though multiple scattering is often insignificant for airborne radar observations of warm rain systems, some heavily precipitating shallow cumulus observed during ORACLES 2017 generated large attenuation and MS may have occasionally occurred. However, MS is generally negligible for the vast majority of APR-3 profiles due to the radar's much narrower field of view compared to *CloudSat*. Evaporation below cloud base is modeled following Comstock et al. (2004) and Feingold (1993). The algorithm typically iterates 5–10 times before converging on a solution (i.e., an LWC profile).

Finally, surface and profile precipitation rate are computed from LWC assuming the fall speed relationship according to Gunn and Kinzer (1949). Following this algorithm, typical uncertainties in instantaneous single-pixel precipitation rate are usually on the order of 100 to 150% for precipitation rates more than 0.1 mm h^{-1} , with higher uncertainty (often above 200%) for much lower rates. Figure 3 presents an example of an APR-3 W-band rainfall retrieval for the convective cell shown in Fig. 2. Between 40 and 60 km from the beginning of the scan, where thin StCu is present, measured reflectivities of -20 to -10 dBZ correspond to retrieved LWC values between 0.005 and 0.01 g m^{-3} . Light precipitation is occurring between 21 and 28 km, with surface rainfall rates peaking at around 0.1 mm h^{-1} . The maximum attenuation corrected profiles in these columns peak at between 20 and 25 dBZ , which closely matches the reflectivity measured at Ka band in Fig. 2. In some profiles, the corresponding LWC values become very large due to the magnification of errors as the algorithm corrects

reflectivity lower in the profile (Hitschfeld and Bordan 1954). Regardless, the retrieved surface rainfall rates remain reasonable given that the surface attenuation-corrected reflectivities are typically between -10 and 5 dBZ .

d. Estimated inversion strength

A large number of metrics could be implemented to account for meteorological controls and context and will be the topic of other ORACLES related studies. For this work, we adopt EIS, which describes the strength of the inversion above the PBL by accounting for temperatures at 700 hPa and the surface (Wood and Bretherton 2006). EIS is computed as

$$\text{EIS} = \text{LTS} - \Gamma_m^{850}(z_{700} - \text{LCL}),$$

where LTS is the lower tropospheric stability or the difference in potential temperature between 700 hPa and the surface, Γ_m^{850} is the moist adiabatic lapse rate at 850 hPa , and LCL is the lifting condensation level. We use ERA-I data to compute EIS. A table of both EIS and LTS, averaged over the first, third, and fifth quintiles (i.e., beginning 20%, middle 20%, and last 20%) of each flight are provided in the appendix.

4. Summary of clouds and precipitation

APR-3 data collected during ORACLES 2016 and 2017 reveal unique cloud and precipitation characteristics with respect to each campaign. An exhaustive summary of cloud and precipitation data collected by the APR-3 and featured in the 2C-RAIN dataset can be found in Tables 3 and 4 (2016 and 2017, respectively). For all analysis in the remaining sections, we use only valid radar profiles, where a valid radar profile is defined as

- 1) occurring during a *level* flight leg, where a level flight leg is defined as a time when the aircraft pitch, drift and roll angles are all less than 3° ; and
- 2) cloud-top altitude is greater than 200 m , which is approximately the lowest altitude before ground clutter contamination becomes an issue.

For all analysis involving estimates of precipitation intensity, we further restrict our analysis using the following flags, which follow the descriptions found in the *CloudSat 2C-RAIN-PROFILE* product manual (Lebsack 2011):

- 1) precipitation flag of 1 (i.e., certain rain or drizzle, lower uncertainty) or 3 (i.e., likely drizzle, higher uncertainty, see below),

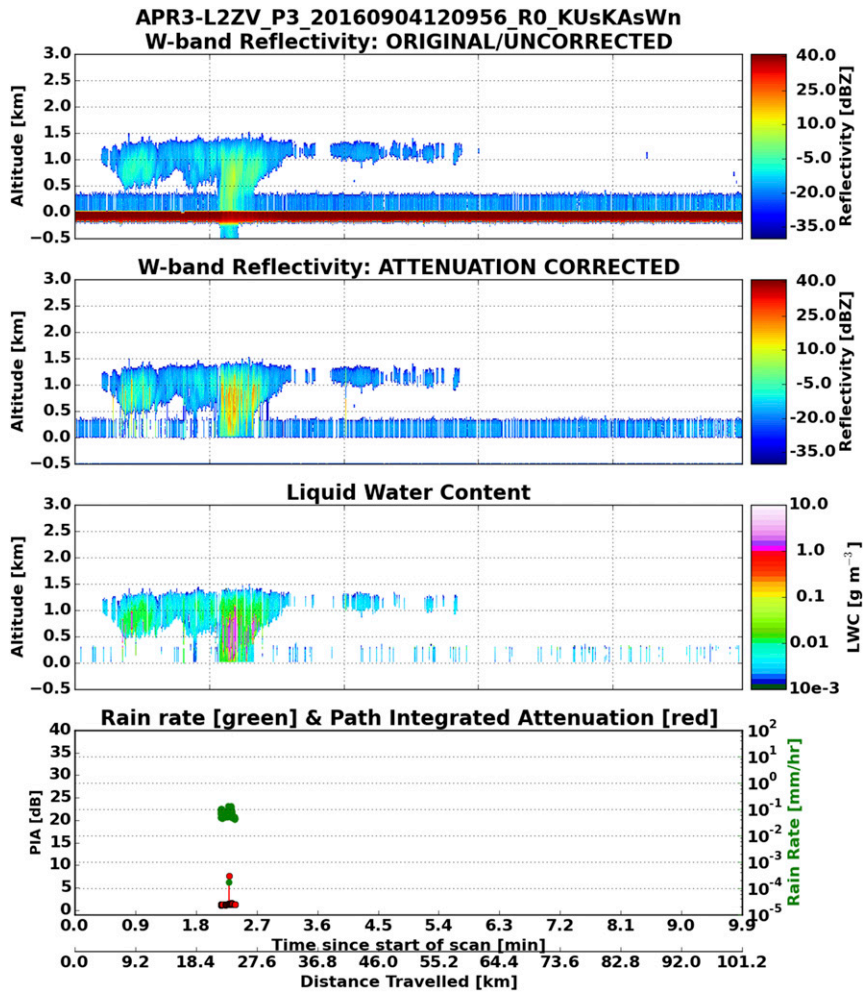


FIG. 3. As in Fig. 2, but with (top) W-band reflectivity, (top middle) attenuation-corrected reflectivity, (bottom middle) liquid water content, and (bottom) surface rain rate and path-integrated attenuation, where the attenuation-corrected reflectivity, LWC, PIA, and surface rain rate are derived from 2C-RP. Rain rate and PIA are plotted only where a valid cloud top above 200 m is found, the retrievals are *high confidence*, and certain rain is present.

- 2) status flag of 0 (i.e., rain-rate estimates from 2C-RP only), and
- 3) quality flag of 4 (i.e., high-quality retrieval).

Retrieved rain rates from profiles with a precipitation flag of 3 typically have much higher uncertainties than those with a precipitation flag of 1. Profiles with a precipitation flag of 3 are included because excluding them would result in grossly underestimated rain fraction statistics due to the vast number of weakly drizzling profiles collected during both experiments.

The next two subsections highlight interesting cloud and precipitation characteristics for specific research flights, as well as similarities among selected research flights from each campaign. A *routine flight* in 2016

references any flight track between Walvis Bay, Namibia, and approximately 10° south latitude and 0° longitude (10°S, 0°), while any *routine flight* in 2017 implies a flight from São Tomé along the 5°E longitude line. A *circuit* or “*suitcase*” flight refers to any series of flights between Namibia–São Tomé and Ascension Island (the latter being located at 7.94°S and 14.35°W), respective to the campaign year, where the first flight ends at Ascension Island and the last flight ends at Namibia–São Tomé. The aforementioned coordinates will be referred to as the “turnaround point” with respect to each campaign hereafter. A summary of the APR-3 data collected (i.e., when the APR-3 was operating) along each flight track for 2016 and 2017 is shown in Fig. 4.

TABLE 3. Daily rainfall statistics for ORACLES 2016. The number of cloudy profiles refers to any *valid* profile where the aircraft was flying a level leg (i.e., a pitch, drift, and roll angle less than 3°) and detected a valid reflectivity profile after noise removal (described in the text). A rejected profile refers to any radar profile that either saw clear skies or was collected during a nonlevel flight leg. The cloud fraction column includes only APR-3 W-band nadir data. The percent of cloudy profiles with virga or surface rainfall account for *valid* cloudy-sky profiles only. The five columns from the right account for only profiles where surface rainfall was present.

	Date	Cloud-top height (mean \pm std)	No. of cloudy profiles (No. of rejected profiles)	Overall cloud fraction (%)	% of cloudy profiles with virga	% of cloudy profiles with surface rainfall	% of cloudy profiles with <0.01 mm h $^{-1}$	Light drizzle	Moderate drizzle (0.01 to 0.1 mm h $^{-1}$)	Heavy drizzle (0.1 to 1.0 mm h $^{-1}$)	Rain (1.0 to 5.0 mm h $^{-1}$)	Heavy rain (>5.0 mm h $^{-1}$)
RF01	31 Aug 2016	0.94 \pm 0.39 km	9733 (159 392)	84.61%	16.74%	21.46%	52.99%	32.17%	11.54%	1.48%	0.62%	
RF02	2 Sep 2016	0.99 \pm 0.18 km	40 702 (105 610)	99.16%	4.08%	71.93%	37.87%	55.21%	4.56%	0.52%	1.23%	
RF03	4 Sep 2016	0.95 \pm 0.22 km	110 793 (198 645)	79.50%	21.26%	47.99%	66.59%	32.04%	1.34%	0.02%	0.01%	
RF04	6 Sep 2016	0.86 \pm 0.16 km	14 504 (166 717)	77.10%	3.41%	67.75%	64.46%	30.01%	5.29%	0.17%	0.06%	
RF05	8 Sep 2016	0.84 \pm 0.42 km	16 269 (342 208)	44.65%	17.17%	34.54%	93.29%	5.64%	1.01%	0.05%	0.00%	
RF06	10 Sep 2016	1.21 \pm 0.23 km	5382 (214 132)	44.08%	44.00%	25.49%	62.39%	33.16%	9.48%	1.75%	1.38%	
RF07	12 Sep 2016	1.13 \pm 0.27 km	66 542 (250 391)	77.00%	30.23%	18.27%	76.46%	21.39%	2.07%	0.04%	0.03%	
RF08	14 Sep 2016	0.86 \pm 0.09 km	7347 (339 770)	81.90%	8.09%	29.21%	88.44%	9.74%	1.21%	0.61%	0.00%	
RF09	18 Sep 2016	0.86 \pm 0.27 km	1596 (183 456)	67.06%	4.74%	7.39%	66.95%	15.25%	0.85%	6.78%	5.93%	
RF10	20 Sep 2016	0.57 \pm 0.07 km	8869 (231 713)	82.44%	3.51%	41.99%	86.11%	11.41%	0.67%	0.19%	0.26%	
F11	24 Sep 2016	0.98 \pm 0.21 km	20 374 (400 020)	68.50%	25.86%	51.30%	47.21%	51.47%	1.22%	0.01%	0.04%	
RF12	25 Sep 2016	1.03 \pm 0.17 km	100 211 (443 338)	96.80%	50.03%	7.40%	59.48%	28.30%	10.81%	0.70%	0.36%	
RF13	27 Sep 2016	1.11 \pm 0.18 km	7673 (230 505)	59.11%	49.16%	44.12%	21.77%	27.83%	17.93%	19.97%	11.31%	
Total			409 995 (3 265 897)	30.55%	34.33%	60.05%	35.00%	3.43%	0.71%	0.59%	0.59%	

TABLE 4. As in Table 3, but for ORACLES 2017.

	Date	Cloud-top height (mean \pm std)	No. of cloudy profiles (No. of rejected profiles)	Overall cloud fraction (%)	% of cloudy profiles with virga	% of cloudy profiles with surface rainfall	Moderate drizzle (0.01 to 0.1 mm h $^{-1}$)	Light drizzle (<0.01 mm h $^{-1}$)	Heavy drizzle (0.1 to 1.0 mm h $^{-1}$)	Rain (1.0 to 5.0 mm h $^{-1}$)	Heavy rain (>5.0 mm h $^{-1}$)
RF01	12 Aug 2017	—	—	—	—	—	—	—	—	—	—
RF02	13 Aug 2017	1.32 \pm 0.24 km	61 961 (490 216)	46.74%	69.71%	6.60%	50.41%	29.88%	3.91%	9.39%	6.38%
R03	15 Aug 2017	1.12 \pm 0.12 km	57 890 (426 529)	45.60%	34.70%	2.45%	72.99%	26.38%	0.63%	0.00%	0.00%
RF04	17 Aug 2017	1.63 \pm 0.31 km	36 857 (602 037)	23.08%	60.19%	9.21%	69.00%	23.78%	3.04%	2.03%	1.52%
RF05	18 Aug 2017	1.45 \pm 0.47 km	4419 (319 207)	11.77%	38.59%	27.36%	49.88%	38.13%	5.71%	1.82%	3.48%
RF06	19 Aug 2017	—	—	—	—	—	—	—	—	—	—
RF07	21 Aug 2017	1.13 \pm 0.26 km	53 230 (521 967)	40.17%	45.32%	12.27%	58.08%	35.85%	3.93%	1.52%	0.53%
RF08	24 Aug 2017	1.60 \pm 0.67 km	73 071 (376 320)	55.22%	43.69%	5.85%	27.80%	8.57%	12.77%	6.86%	41.72%
RF09	26 Aug 2017	1.28 \pm 0.38 km	16 695 (631 397)	25.12%	42.48%	29.68%	52.19%	25.45%	7.04%	5.37%	9.88%
RF10	28 Aug 2017	1.36 \pm 0.36 km	82 104 (833 139)	53.55%	38.43%	26.37%	46.55%	47.17%	5.94%	0.27%	0.05%
RF11	30 Aug 2017	1.28 \pm 0.17 km	174 202 (762 926)	61.36%	59.28%	15.77%	42.17%	39.93%	14.28%	1.81%	1.60%
RF12	31 Aug 2017	1.49 \pm 0.18 km	10 708 (617 743)	46.41%	50.63%	7.96%	34.98%	44.60%	19.01%	0.59%	0.82%
Total			604 822 (5 581 481)	51.38%	13.28%	46.89%	37.44%	9.05%	2.23%	4.11%	

a. Summary of ORACLES 2016

The first research flight (RF) of ORACLES 2016 took place on 31 August 2016. Stratocumulus clouds persisted from the coast to the turnaround point with some StCu exhibiting a more distinct cellular structure closer to the target point. Near the coast during the beginning of the flight, EIS exceeded 11 K but decreased to 6.4 K out at the turnaround point (Fig. 5, also see Table A1). Clouds were observed in 85% of all W-band radar measurements (Table 3) and most precipitation rates were very light, with over 53% of retrieved precipitation rates less than 0.01 mm h $^{-1}$.

The second RF, taking place 2 September 2016, featured over 99% cloud fraction estimated by the W band—the highest for the campaign. Nearly 72% of all cloudy profiles were observed to be precipitating. A distinct upper level low over the central South Atlantic, which formed on 1 September 2016, began building north and east on this day. Although RF02 took place mostly near the coast, a transition from a mostly homogeneous StCu deck (i.e., a cloud deck with no distinct open- or closed-cell structure apparent) to a closed-cell StCu deck became more apparent. By 4 September 2016 (RF03), the aforementioned low had begun to weaken but moved east of the prime meridian, resulting in the least dynamically stable day of the entire campaign. This is evident in satellite imagery (not shown) showing that the StCu deck did not extend farther than about 8E on 4 September 2016. The turnaround point was mostly devoid of cloud, which is manifested in the APR-3 lower observed cloud fraction relative to RF01 four days prior. The combined virga and rain fraction for RF03 was also much higher than that of RF01.

By 6 September 2016 (RF04), the StCu deck recovered over much of the SE Atlantic basin. Much of the StCu present this day was closed-cell with a similar cloud fraction as RF03 but with a higher rain fraction. Interestingly, precipitation rates (Table 3, columns 7–9) are quite similar between these two flights, though greater percentages of heavy drizzle, light rain, and heavy rain are noted for RF04.

Research flights 05, 06, and 07 followed the routine flight track, observing nearly the same curtain in the SE Atlantic Ocean over a period of five days. For RF05 on 8 September 2016, the StCu deck thinned out under very stable conditions with EIS exceeding 9 K for the entire flight (see Table A1). Cloud fraction, rain fraction, and overall intensity dramatically decreased between this flight and RF04 two days earlier. RF06 had similar stability conditions, although open-cell StCu was more apparent on this day. RF07 also had similar EIS, with

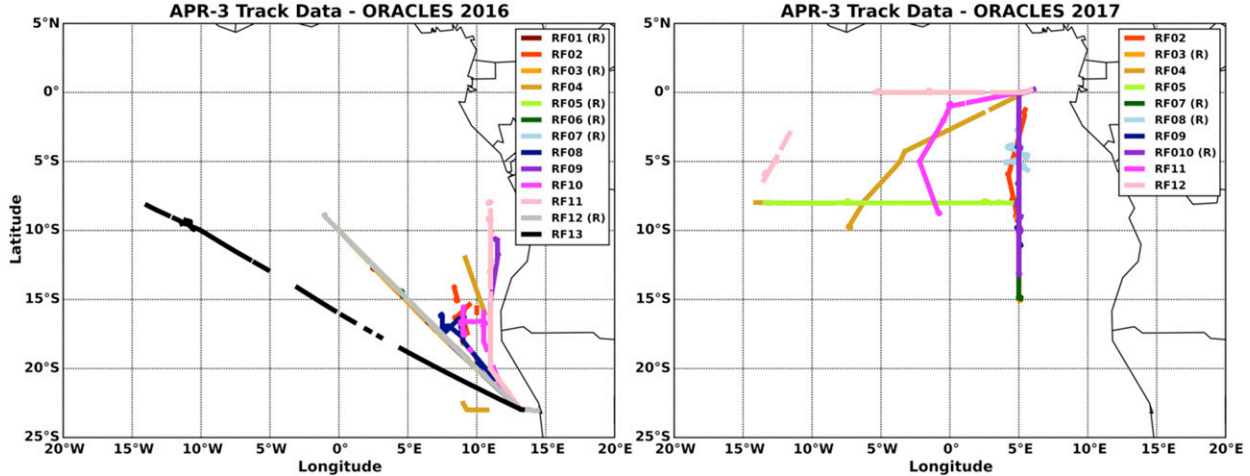


FIG. 4. APR-3 data collection lines from the (left) 2016 and (right) 2017 campaigns. The (R) denotation represents flights that approximately followed the routine flight track for that campaign year and thus overlap one another.

values of 8.5 K or higher frequently occurring. This flight was different from RFs 05 and 06 in that 77% of profiles from RF07 had observable cloud cover, compared to around 44% for RFs 05 and 06. The frequency of virga was highest for RF06, but the fraction of precipitating profiles gradually decreased from 34.5% on RF05 to 18.3% on RF07.

The next series of flights, RFs 08, 09, and 10, all took place near the coast. Despite the APR-3 collecting at least 180 000 profiles from each of these flights, fewer than 10 000 profiles satisfied the filtering criteria. On 14 September 2016 (RF08), the APR-3 observed perhaps the most homogeneous StCu cloud deck of the entire campaign: the standard deviation of cloud-top altitudes was only 0.09 km. Between RFs 09 and 10, the mean cloud-top altitude decreased from 0.86 to 0.57 km between the two days with the standard deviation of cloud-top altitudes decreasing from 0.27 to 0.07 km. This was likely due to most of the measurements being collected south of 15°S, where SSTs were cooler (not shown) and thus more conducive for a shallower PBL. All three flights had virga fractions of less than 9%, and the majority of surface precipitation intensities were less than 0.01 mm h^{-1} .

A suitcase flight took place 24–25 September 2016 (RFs 11 and 12). These two flights were among the most successful for APR-3 data collection, with the 25 September 2016 flight featuring the highest collection of valid 2C-RP surface precipitation data. Cloud-top altitudes were very similar to the mean, varying by only 0.05 km between the two days. W-band-derived cloud fraction increased substantially from RF11 to RF12 (69%–97%) but precipitation frequency dramatically decreased from 51% to 7%. Given the decrease in

moderate drizzle from RF11 to larger percentages of light drizzle and heavy drizzle in RF12, and noting that many clouds were observed in the same portion of the basin, we suspect StCu cloud dissipation was occurring. This idea will be the topic of future research, since we do not fully investigate temporal changes in cloud and precipitation processes during either experiment.

The final research flight of the 2016 campaign (RF13) featured the largest percentages of heavy drizzle and rain—evidenced by frequent W-band attenuation (not shown) and significant radar returns in the Ka band and

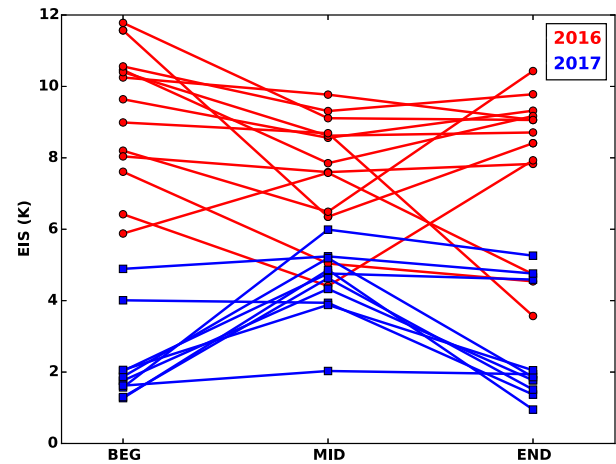


FIG. 5. Estimated inversion strength (EIS) along the ORACLES 2016 (red) and 2017 (blue) flight tracks. Each dot (2016) or square (2017) represents the average EIS for the beginning 20% of the flight (i.e., starting when the APR-3 was turned on), middle 20% of the flight, and ending 20% (i.e., ending when the APR-3 was turned off) of the flight.

sometimes the Ku band. Most of these cases are from convective cumulus near Ascension Island.

b. Summary of ORACLES 2017

APR-3 data collection for the ORACLES 2017 campaign began with research flights 02 and 03 (15 and 17 August 2017). RF02 featured one of the lowest rain fractions of the campaign with only 6.6% of cloudy, level legs precipitating. RF03 had a very similar cloud fraction (45.6% compared to 46.7% from RF02) yet only 2.5% of all profiles were precipitating. Nearly all of the precipitating profiles collected during this day contain either light or moderate drizzle (Table 4). A comparison of satellite imagery from between these two days shows a slight southward retreat of the StCu deck, with many more instances of open-cell StCu observed during RF03.

The next three flights (RF04, RF05, and RF07 on 17, 18, and 21 August 2017) were a series of flights taking place from São Tomé to Ascension Island and back, with RF05 beginning and ending at Ascension Island. The flight path for RF04 skirted along the northwestern flank of the cloud deck and StCu to Cu transition zone (Fig. 4), which is likely why the APR-3 only estimated a 23.1% cloud fraction. Cloud-top heights during RF04 were also the highest of the 2017 campaign, with a mean cloud-top altitude of 1.63 km. Overall, 9.2% of the valid profiles were precipitating with many of these profiles being light drizzle with precipitation rates under 0.01 mm h^{-1} . The StCu deck expanded northward in time for RF05, however, only about 4400 out of the approximately 319 000 collected profiles (or $\sim 1\%$) were valid. RF05 featured the lowest cloud fraction estimate (11.8%) observed by the APR-3 during the 2017 campaign. RF07 saw both an increase in estimated cloud fraction (40.2%) and rain fraction (12.3%) with the second lowest mean cloud-top altitude (1.13 km) for the 2017 campaign. The majority of the measurements were taken in the StCu deck along 8°S and the northern part of the routine flight track along 5°E . Even though the StCu deck on this day appeared to contain more open-cell StCu compared to the other days, close to 94% of the precipitation rate estimates fell in the light/moderate drizzle categories rather than in the heavy drizzle or rain categories.

RF08, taking place on 24 August 2017, contained arguably the most diverse range of cloud and precipitation characteristics. The APR-3 estimated a mean cloud-top altitude of 1.6 km and a cloud-top standard deviation of approximately 0.7 km. The observed rain fraction on this day was especially diverse, with 28%, 13%, and 42% of surface precipitation rates in the light drizzle, heavy drizzle, and heavy rain categories, respectively. RF09, by comparison, was a target of opportunity flight that

only reached about 6°S . The cloud deck was fairly expansive and homogeneous on this day, but similar to RF05, the aircraft only flew into the northernmost portion of the cloud deck and hence the APR-3 estimated a lower cloud fraction of 25.1%. A notable number of profiles were collected near the equator that measured heavy drizzle or rain, accounting for about 22% of precipitating profiles for RF09.

The final routine flight of the 2017 campaign took place on 28 August 2017. RF10 had a similar rain fraction as RF08 but had over double the cloud fraction. Most of the profiles collected during this day were in a mostly closed-cell StCu deck, with a mean cloud-top altitude around 1.36 km. Close to 26.4% of level, cloudy-sky profiles were precipitating and over 93% of these profiles were either in the light or moderate drizzle categories.

The final two flights, RFs 11 and 12 on 30 and 31 August 2017, respectively, were a pair of target of opportunity flights designed such that RF12 would resample clouds and aerosols from RF11. The APR-3 observed over 170 000 valid cloudy-sky profiles during RF11, which was the most of the 2017 campaign. Over 80% of surface precipitation rates were in the light or moderate categories, yet a large number of heavy drizzle cases (14.3%) were collected too. The next flight, RF12, followed a track farther north and west compared to RF11. The StCu deck slightly retreated to the south and east, with much of the deck appearing more open-cell in character. Both cloud and rain fractions were much lower in RF12 than RF11 although a larger percentage of moderate and heavy drizzle cases were taken.

5. Discussion

Addressing ORACLES primary science objectives, which include assessing cloud morphology and precipitation trends in the SE Atlantic StCu deck, requires accurate knowledge of the *environmental* regimes sampled during each research flight. Using EIS as a crude proxy for local thermodynamic conditions, significantly different conditions prevailed during the 2016 and 2017 campaigns.

Throughout the 2016 campaign, EIS was strong near the coast (east of 10°E), often exceeding 11 K from the central Namibian coast through the Namibia–Angola border (Fig. 6). EIS decreased to about 6 K at the turnaround point for routine flights. By comparison, only the middle portions of RF04 and RF10 had an $\text{EIS} \geq 5 \text{ K}$ during the entire 2017 campaign. West of 0°E during 2016, EIS sometimes decreased below 4 K during certain flights where a larger number of light to heavy rain scenes were observed (e.g., RF13 with the largest

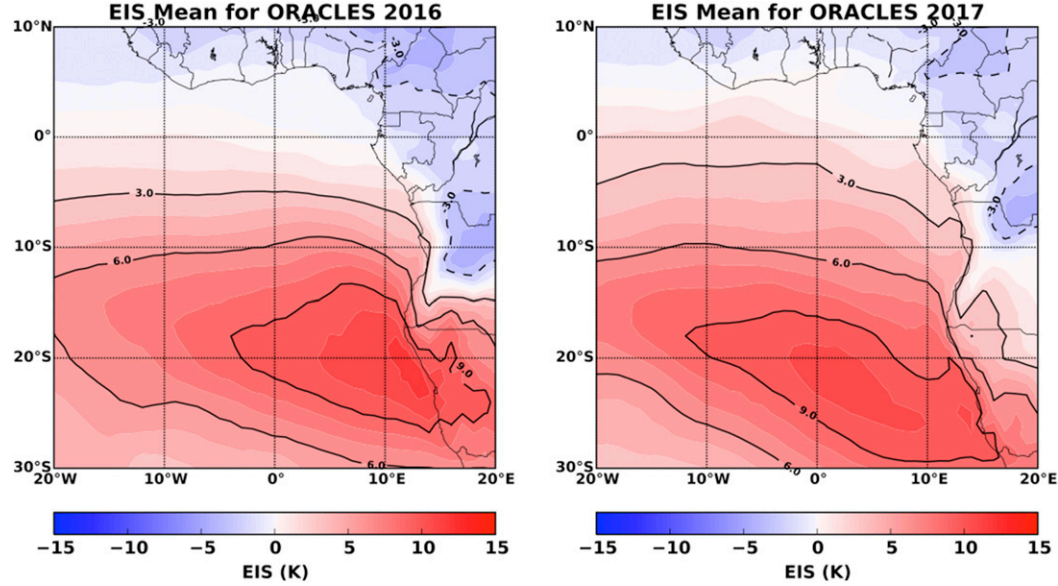


FIG. 6. Mean daytime estimated inversion strength (EIS) for the ORACLES (left) 2016 and (right) 2017 campaigns. EIS is computed from ERA-I reanalysis data following the methodology outlined in [Wood and Bretherton \(2006\)](#). To assure daytime-only data are used, 1200 UTC data are used in this figure.

percentage of rain or heavy rain cases, see [Table 3](#)). The middle of RF11, as well as the end of RFs 12 and 13, occurred when EIS was near its lowest values for the campaign ([Fig. 5](#), also see [Table A1](#)). In contrast, the entirety of research flights 2, 4, 6, 7, and 8 (for 2016) occurred in regimes where EIS exceeded 8 K, representing a very stable lower troposphere and strong inversion. While this analysis suggests clear geographic variability in EIS during each year, we again cannot make conclusions at this time that *temporal* variability in EIS was primarily responsible for the observed differences in cloud and precipitation characteristics.

Differences in cloud fraction and structure were noted during both campaigns. During the 2016 campaign, cloud-top altitudes varied from approximately 0.80 to 0.90 km near the Namibian coast to higher than 1.30 km at the turnaround point ([Fig. 7a](#)). Many cloud-top altitudes exceeded 1 km altitude (sometimes higher than 1.4 km) in 2017. The increase in cloud-top altitude is associated with an increase in PBL depth west of the African coast, which is in turn associated with a gradient in sea surface temperatures (PBL depth is especially shallow near the African coast due to coastal upwelling). Cloud depths ([Fig. 7](#)) estimated from the APR-3 (with cloud base being defined as the lowest altitude with a valid reflectivity measurement) were typically a few hundred meters. The cloud fraction from each flight in 2016 typically agreed with climatological values of cloud fraction over the primary experiment area (e.g., [Fig. 5](#) in [Adebiyi et al. 2015](#)). Cloud fraction estimates during

2017, by contrast, were lower than climatology for most flights. The most common reflectivity measurements taken by the W-band radar were between -20 and -10 dBZ and typically occurred below 1 km ([Fig. 8](#)), further showing that many of the observed StCu clouds were typically a couple hundred meters thick. Only trade cumulus observed near Ascension Island and close to the equator account for any cloud-top altitudes above 2 km. The results shown in [Fig. 8](#) corroborate previous findings (e.g., [Liu et al. 2015](#)) that many StCu measurements occur in *CloudSat's* blind zone, which is about 720 m above ground level.

Precipitation statistics for the ORACLES 2016 and 2017 campaigns are summarized in [Fig. 9](#). For all valid cloudy profiles, approximately 35% of all profiles are not precipitating for both campaigns, and over 98% (2016) and 93% (2017) of precipitating profiles have surface precipitation rates of less than 1.0 mm h^{-1} ([Fig. 9](#)). The mode of observed precipitation rates of less than 0.1 mm h^{-1} are consistent with estimates found in other observational (e.g., [Austin et al. 1995](#)) and modeling (e.g., [Stevens et al. 1998](#)) studies. In general, we find approximately 34% of all observed cloudy profiles contained surface precipitation in 2016, whereas only 13% of profiles included surface precipitation in 2017. Rain fraction estimates for both years are somewhat higher than those found in previous climatological studies utilizing *CloudSat* (e.g., [Fig. 3](#) in [Ellis et al. 2009](#); [Fig. 4](#) in [Kay et al. 2018](#)), where these studies found observed rain fraction estimates between 0.04 and 0.12. Given that most observations in 2017 were taken farther

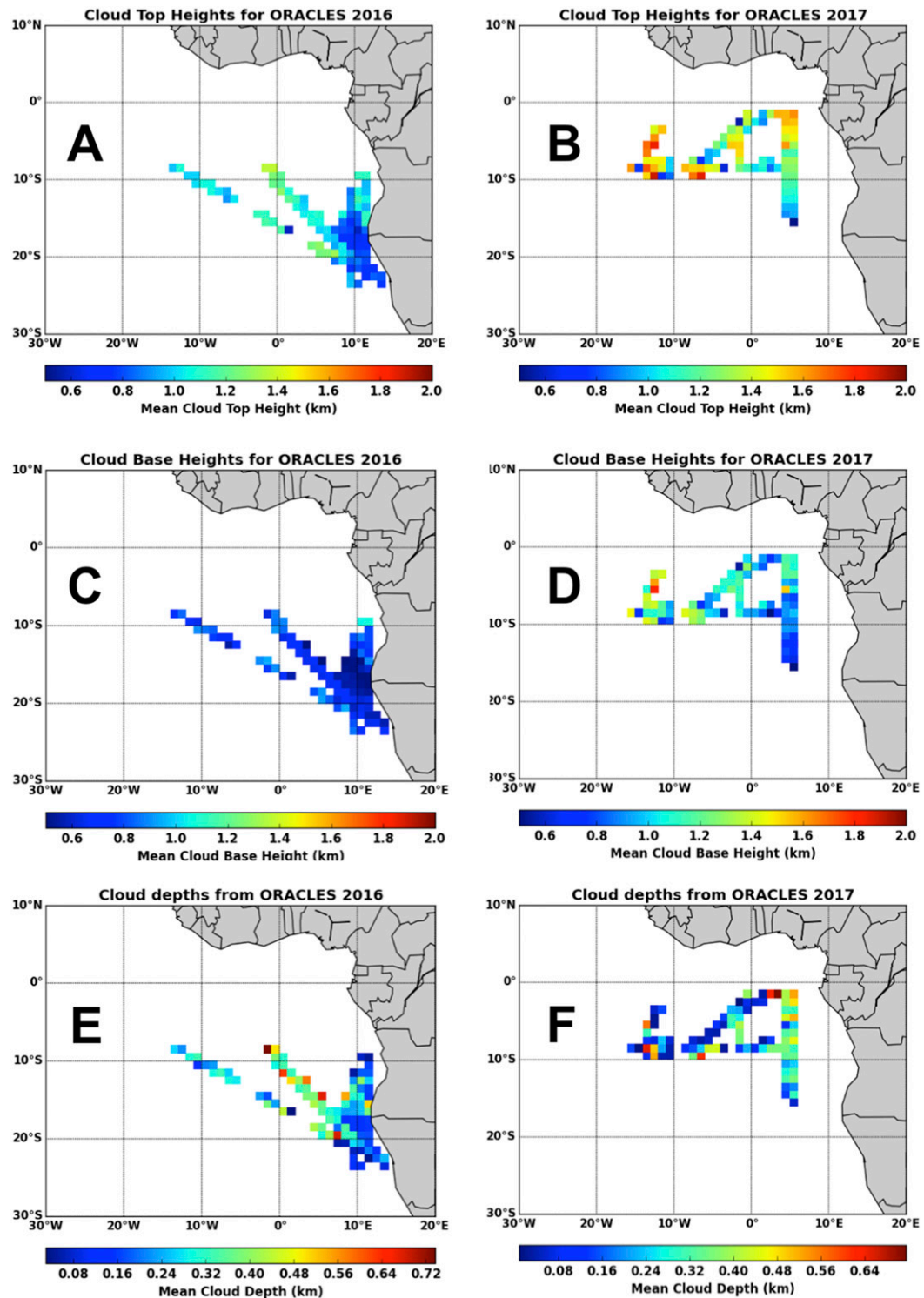


FIG. 7. APR-3 W-band estimated cloud-top altitudes [(a) 2016, (b) 2017], cloud-base altitudes [(c) 2016, (d) 2017], and cloud depths [(e) 2016, (f) 2017] in the SE Atlantic basin. Cloud depth is the difference between cloud-top altitude and cloud-base altitude, with cloud-base altitude assumed to be the lowest altitude in the cloud with a valid radar reflectivity measurement. Data are binned according to $1^\circ \times 1^\circ$ latitude-longitude boxes.

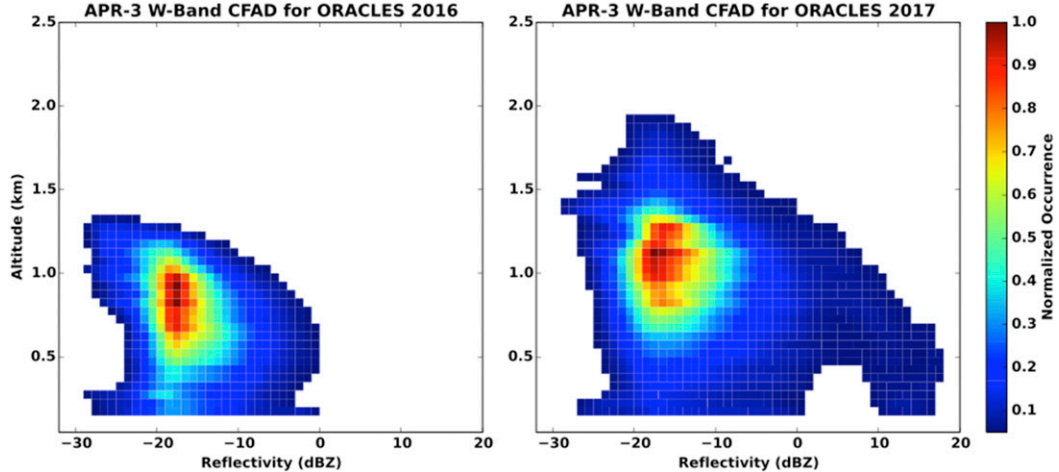


FIG. 8. Normalized frequency by altitude diagram of attenuation-corrected W-band reflectivity measurements for ORACLES (left) 2016 and (right) 2017.

north and west in the SE Atlantic Ocean and in environments where EIS was (on average) several degrees less, and noting that more rain rates above 1 mm h^{-1} were also observed, we suspect the APR-3 observed more open-cell StCu during this year.

Temporal variability is more difficult to evaluate using ORACLES observations and is not addressed in this study. During ORACLES 2016 and 2017, clouds and precipitation are observed throughout the morning and afternoon portions of the diurnal cycle. One avenue to potentially address the temporal evolution of clouds and precipitation would involve the analysis of “square spiral” flight pattern data, which exist for most research flights. In these flight legs, the APR-3 collected data along four distinct descending but level “walls” and was measured over the course of about 10 min. In-cloud observations in at least one of these walls often succeeded the conclusion of the square spiral descent further presenting a possible avenue for validating retrieved water contents and rainfall rates against in situ derived rainfall rates from cloud probe data. The opportunities for such analyses are, however, quite limited since the clouds sampled earlier in a flight will not necessarily represent conditions observed later in a flight. The assessment of temporal variability in clouds and precipitation during the ORACLES experiment, validation of the retrieval products, and subsequent analysis on cloud-aerosol–precipitation interactions are beyond the scope of the present study but will be the topic of future investigation.

6. Conclusions

This paper summarizes the macrophysical character of clouds and precipitation observed during ORACLES

2016 and 2017 based on rainfall rate retrievals from APR-3 W-band radar observations. With vertical resolution as high as 8.3 m and over 10 million profiles taken between the two campaigns, this dataset offers an extensive airborne radar dataset for studying StCu clouds and warm precipitation processes over the southeast Atlantic Ocean. The high sensitivity of the APR-3 W band provides accurate depictions of rainfall frequency and cloud fraction. Utilizing an optimal estimation algorithm—with robust physics and accounting of all relevant sources of uncertainty—mitigates a number of challenges associated with quantifying precipitation rates from attenuating radars though uncertainties in the precipitation *intensity* estimates can be large owing to the single-frequency nature of the retrieval.

Even though the rain fraction for 2016 was more than twice that observed in 2017, the combined virga plus conditional rain rates between both campaigns are strikingly similar (Fig. 9) at approximately 65%. This number may be biased a bit high due to the fact that the APR-3 W band lacked sensitivity to the thinnest clouds observed by other collocated remote sensors, and will be explored in future work. In general, we find no obvious trends when comparing cloud fraction with rain and virga fraction between the two campaigns. Surface rainfall intensity, however, generally increases west of the African coast. APR-3 estimated cloud fraction also generally decreases away from the coast for both years, and, given how rainfall intensity changes away from the coast as well, this finding is consistent with the presence of more open-cell StCu forming in a deeper planetary boundary layer. Of the 10 million profiles collected between the two campaigns, over one million of these profiles satisfied our validation criteria.

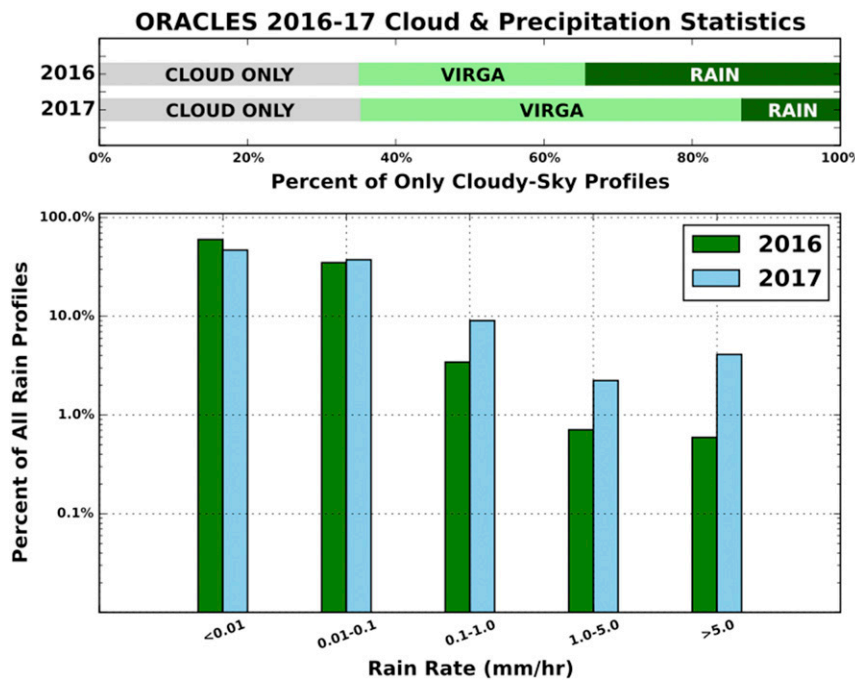


FIG. 9. ORACLES 2016 and 2017 campaign (top) cloud-only (gray), virga-only (light green), and drizzling/raining profiles (dark green) for *all* cloudy-sky profiles where the aircraft was flying at nadir. (bottom) Retrieved rainfall rates for all drizzling or raining profiles for 2016 (green) and 2017 (blue) are binned by intensity. CLOUD represents the fraction of all cloudy-sky profiles that did not have virga nor precipitation, and VIRGA represents the fraction of all cloudy profiles with a maximum reflectivity of -15 dBZ or greater anywhere in the column.

EIS was high (exceeding 8–10 K) near the Namibian coast throughout much of the ORACLES 2016 campaign and decreased by, on average, 4 K at the routine flight turnaround marker. Most of the research flights in 2017 flew in environments where EIS was, on average, 5 K or less. This results in lower mean cloud-top altitudes near the coast in 2016 (0.8–0.9 km) compared to upward of 1.3 km farther west in 2016 and for most cases in 2017. For 2017, EIS generally increased from near 1–2 K to above 4 K at the routine flight turnaround point as well as the turnaround point for various target of opportunity flights. We note that SST and LTS variability in the SE Atlantic, especially in the StCu–Cu transition region, are important controls on cloud-top altitude and will require further investigation. Given the environmental stability differences between the two campaigns as well as the geographical differences in cloud-top altitudes and structure, the vast quantity of data available will enable extensive study of cloud–aerosol–precipitation interactions in distinct environments.

These results highlight only a fraction of the interesting data collected during ORACLES 2016 and 2017. In addition to providing valuable insights into cloud–aerosol interactions in this unique environment, in situ data collected during both campaigns can be used

to define instrument requirements for future satellite missions, validate retrieval algorithm assumptions, and evaluate their impact on liquid water content and above-surface precipitation rate retrievals. These analyses will be critical toward ensuring accurate assessments of cloud–aerosol interactions as they relate to cloud and precipitation processes, and toward improving future spaceborne satellite radar missions.

Acknowledgments. The authors thank Steve Durden, Elin McIlhattan, Greg Sadowsy, Gregg Dobrowalski, William Chun, Raquel Rodriguez Monje, and Matt Lebsack for assisting with APR-3 data collection, hardware support, and data processing. A portion of the research described in this paper was performed at the Jet Propulsion Laboratory, California Institute of Technology, under contract with the National Aeronautics and Space Administration. The authors would also like to thank the ORACLES science team for multiple insightful discussions that led to the creation of the dataset described in this paper. Finally, the authors thank Mikael Witte and two anonymous reviewers for their constructive and insightful comments that vastly improved the quality of this manuscript. This work was funded under NASA Grant NNX15AF99G.

TABLE A1. Estimated inversion strength and lower tropospheric stability partitioned by the beginning 20%, middle 20%, and ending 20% of each flight for the ORACLES (left) 2016 and (right) 2017 experiments.

ORACLES 2016	EIS_BEG (K)	EIS_MID (K)	EIS_END (K)	LTS_BEG (K)	LTS_MID (K)	LTS_END (K)	ORACLES 2017	EIS_BEG (K)	EIS_MID (K)	EIS_END (K)	LTS_BEG (K)	LTS_MID (K)	LTS_END (K)
RF01 31 Aug 2016	11.57	6.35	8.41	28.17	23.39	25.22	RF01 12 Aug 2017	—	—	—	17.60	19.91	18.02
RF02 2 Sep 2016	9.64	8.56	9.32	26.34	26.06	26.57	RF02 13 Aug 2017	1.76	4.33	1.77	17.58	20.89	20.52
RF03 4 Sep 2016	8.20	6.49	10.43	24.61	23.40	26.58	RF03 15 Aug 2017	2.03	4.76	4.59	16.82	20.76	19.67
RF04 6 Sep 2016	10.25	9.77	9.06	24.60	26.57	25.93	RF04 17 Aug 2017	1.57	5.99	5.26	—	—	—
RF05 8 Sep 2016	10.46	7.85	9.17	26.14	24.17	24.95	RF05 18 Aug 2017	4.89	5.24	4.76	20.04	20.25	19.94
RF06 10 Sep 2016	11.78	9.11	9.06	28.00	24.97	26.30	RF06 19 Aug 2017	—	—	—	—	—	—
RF07 12 Sep 2016	10.40	8.62	8.71	26.75	24.89	24.89	RF07 21 Aug 2017	4.01	3.94	1.37	19.38	19.33	17.18
RF08 14 Sep 2016	10.56	9.31	9.78	27.31	25.77	26.63	RF08 24 Aug 2017	1.27	4.86	0.95	17.48	20.69	17.04
RF09 18 Sep 2016	8.99	8.69	3.57	26.07	25.32	19.95	RF09 26 Aug 2017	1.62	2.03	1.94	17.42	17.98	17.80
RF10 20 Sep 2016	8.04	7.60	7.83	24.60	25.13	25.25	RF10 28 Aug 2017	1.87	5.19	1.86	18.08	21.13	18.11
RF11 24 Sep 2016	6.42	4.41	7.93	23.51	20.45	21.15	RF11 30 Aug 2017	1.30	4.63	1.51	17.28	20.89	17.33
RF12 25 Sep 2016	5.88	7.58	4.74	19.44	24.33	15.43	RF12 31 Aug 2017	2.06	3.88	2.05	17.90	20.09	17.89
RF13 27 Sep 2016	7.61	5.04	4.54	22.49	20.52	19.94							

APPENDIX

Estimated Inversion Strength and Lower Tropospheric Stability

Table A1 shows the EIS and LTS, computed from ERA-Interim data for the beginning 20%, middle 20%, and ending 20% of each flight during both the (left) ORACLES 2016 and (right) 2017 experiments.

REFERENCES

- Abel, S. J., and B. J. Shipway, 2007: A comparison of cloud-resolving model simulations of trade wind cumulus with aircraft observations taken during RICO. *Quart. J. Roy. Meteor. Soc.*, **133**, 781–794, <https://doi.org/10.1002/qj.55>.
- , and I. A. Boutle, 2012: An improved representation of the raindrop size distribution for single-moment microphysics schemes. *Quart. J. Roy. Meteor. Soc.*, **138**, 2151–2162, <https://doi.org/10.1002/qj.1949>.
- Adebisi, A. A., P. Zuidema, and S. J. Abel, 2015: The convolution of dynamics and moisture with the presence of shortwave absorbing aerosols over the southeast Atlantic. *J. Climate*, **28**, 1997–2024, <https://doi.org/10.1175/JCLI-D-14-00352.1>.
- Albrecht, B. A., 1989: Aerosols, cloud microphysics, and fractional cloudiness. *Science*, **245**, 1227–1231, <https://doi.org/10.1126/science.245.4923.1227>.
- , C. S. Bretherton, D. Johnson, W. H. Scubert, and A. S. Frisch, 1995: The Atlantic Stratocumulus Transition Experiment—ASTEX. *Bull. Amer. Meteor. Soc.*, **76**, 889–904, [https://doi.org/10.1175/1520-0477\(1995\)076<0889:TASTE>2.0.CO;2](https://doi.org/10.1175/1520-0477(1995)076<0889:TASTE>2.0.CO;2).
- , and Coauthors, 2019: Cloud System Evolution in the Trades (CSET): Following the evolution of boundary layer cloud systems with the NSF–NCAR GV. *Bull. Amer. Meteor. Soc.*, **100**, 93–121, <https://doi.org/10.1175/BAMS-D-17-0180.1>.
- Austin, P., Y. Wang, V. Kujala, and R. Pincus, 1995: Precipitation in stratocumulus clouds: Observational and modeling results. *J. Atmos. Sci.*, **52**, 2329–2352, [https://doi.org/10.1175/1520-0469\(1995\)052<2329:PISCOA>2.0.CO;2](https://doi.org/10.1175/1520-0469(1995)052<2329:PISCOA>2.0.CO;2).
- Battaglia, A., and C. Simmer, 2008: How does multiple scattering affect the spaceborne W-band radar measurements at ranges close to and crossing the sea-surface range? *IEEE Trans. Geosci. Remote Sens.*, **46**, 1644–1651, <https://doi.org/10.1109/TGRS.2008.916085>.
- Bennartz, R., 2007: Global assessment of marine boundary layer cloud droplet number concentration from satellite. *J. Geophys. Res.*, **112**, D02201, <https://doi.org/10.1029/2006JD007547>.
- Berg, W., T. L’Ecuyer, and C. Kummerow, 2006: Rainfall climate regimes: The relationship of regional TRMM rainfall biases to the environment. *J. Appl. Meteor. Climatol.*, **45**, 434–454, <https://doi.org/10.1175/JAM231.1>.
- , —, and J. M. Haynes, 2010: The distribution of rainfall over oceans from spaceborne radars. *J. Appl. Meteor. Climatol.*, **49**, 535–543, <https://doi.org/10.1175/2009JAMC2330.1>.
- Bretherton, C. S., R. Wood, R. C. George, D. Leon, G. Allen, and X. Zheng, 2010: Southeast Pacific stratocumulus clouds, precipitation and boundary layer structure sampled along 20° S during VOCALS-REx. *Atmos. Chem. Phys.*, **10**, 10 639–10 654, <https://doi.org/10.5194/acp-10-10639-2010>.
- Clothiaux, E. E., M. A. Miller, B. A. Albrecht, T. P. Ackerman, J. Verlinde, D. M. Babb, R. M. Peters, and W. J. Syrett, 1995: An evaluation of a 94-GHz radar for remote sensing of cloud

- properties. *J. Atmos. Oceanic Technol.*, **12**, 201–229, [https://doi.org/10.1175/1520-0426\(1995\)012<0201:AEOAGR>2.0.CO;2](https://doi.org/10.1175/1520-0426(1995)012<0201:AEOAGR>2.0.CO;2).
- Comstock, K. K., R. Wood, S. E. Yuter, and C. S. Bretherton, 2004: Reflectivity and rain rate in and below drizzling stratocumulus. *Quart. J. Roy. Meteor. Soc.*, **130**, 2891–2918, <https://doi.org/10.1256/qj.03.187>.
- Cox, S. K., D. S. McDougal, D. A. Randall, and R. A. Schiffer, 1987: FIRE—The First ISCCP Regional Experiment. *Bull. Amer. Meteor. Soc.*, **68**, 114–118, [https://doi.org/10.1175/1520-0477\(1987\)068<0114:FFIRE>2.0.CO;2](https://doi.org/10.1175/1520-0477(1987)068<0114:FFIRE>2.0.CO;2).
- Dee, D. P., and Coauthors, 2011: The ERA-Interim reanalysis: Configuration and performance of the data assimilation system. *Quart. J. Roy. Meteor. Soc.*, **137**, 553–597, <https://doi.org/10.1002/qj.828>.
- Diamond, M. S., and Coauthors, 2018: Time-dependent entrainment of smoke presents an observational challenge for assessing aerosol–cloud interactions over the southeast Atlantic Ocean. *Atmos. Chem. Phys.*, **18**, 14 623–14 636, <https://doi.org/10.5194/acp-18-14623-2018>.
- Ellis, T. D., T. L'Ecuyer, J. M. Haynes, and G. L. Stephens, 2009: How often does it rain over the global oceans? The perspective from CloudSat. *Geophys. Res. Lett.*, **36**, L03815, <https://doi.org/10.1029/2008GL036728>.
- Feingold, G., 1993: Parameterization of the evaporation of rainfall for use in general circulation models. *J. Atmos. Sci.*, **50**, 3454–3467, [https://doi.org/10.1175/1520-0469\(1993\)050<3454:POTEOR>2.0.CO;2](https://doi.org/10.1175/1520-0469(1993)050<3454:POTEOR>2.0.CO;2).
- Gerber, H., 1996: Microphysics of marine stratocumulus clouds with two drizzle modes. *J. Atmos. Sci.*, **53**, 1649–1662, [https://doi.org/10.1175/1520-0469\(1996\)053<1649:MODSCW>2.0.CO;2](https://doi.org/10.1175/1520-0469(1996)053<1649:MODSCW>2.0.CO;2).
- Gunn, R., and G. D. Kinzer, 1949: The terminal velocity of fall for water droplets in stagnant air. *J. Atmos. Sci.*, **6**, 243–248, [https://doi.org/10.1175/1520-0469\(1949\)006<0243:TTVOFF>2.0.CO;2](https://doi.org/10.1175/1520-0469(1949)006<0243:TTVOFF>2.0.CO;2).
- Haynes, J. M., T. L'Ecuyer, G. L. Stephens, S. D. Miller, C. Mitrescu, N. B. Wood, and S. Tanelli, 2009: Rainfall retrievals over the ocean with spaceborne high-frequency cloud radar. *J. Geophys. Res.*, **114**, D00A22, <https://doi.org/10.1029/2008JD009973>.
- Hitschfeld, W., and J. Bordan, 1954: Errors inherent in the radar measurement of rainfall at attenuating wavelengths. *J. Meteor.*, **11**, 58–67, [https://doi.org/10.1175/1520-0469\(1954\)011<0058:EIITRM>2.0.CO;2](https://doi.org/10.1175/1520-0469(1954)011<0058:EIITRM>2.0.CO;2).
- Hogan, R. J., and A. Battaglia, 2008: Fast lidar and radar multiple-scattering models. Part II: Wide-angle scattering using the time-dependent two-stream approximation. *J. Atmos. Sci.*, **65**, 3636–3651, <https://doi.org/10.1175/2008JAS2643.1>.
- Houze, R. A., and Coauthors, 2017: The Olympic Mountains Experiment (OLYMPEx). *Bull. Amer. Meteor. Soc.*, **98**, 2167–2188, <https://doi.org/10.1175/BAMS-D-16-0182.1>.
- Jing, X., K. Suzuki, H. Guo, D. Goto, T. Ogura, T. Koshiro, and J. Mühlstädt, 2017: A multimodel study on warm precipitation biases in global models compared to satellite observations. *J. Geophys. Res. Atmos.*, **122**, 11 806–11 824, <https://doi.org/10.1002/2017JD027310>.
- Kay, J. E., T. L'Ecuyer, A. Pendergrass, H. Chepfer, R. Guzman, and V. Yettella, 2018: Scale-aware and definition-aware evaluation of modeled near-surface precipitation frequency using CloudSat observations. *J. Geophys. Res. Atmos.*, **123**, 4294–4309, <https://doi.org/10.1002/2017JD028213>.
- L'Ecuyer, T. S., and G. L. Stephens, 2002: An estimation-based precipitation retrieval algorithm for attenuating radars. *J. Appl. Meteor.*, **41**, 272–285, [https://doi.org/10.1175/1520-0450\(2002\)041<0272:AEBPRA>2.0.CO;2](https://doi.org/10.1175/1520-0450(2002)041<0272:AEBPRA>2.0.CO;2).
- , W. Berg, J. Haynes, M. Lebsack, and T. Takemura, 2009: Global observations of aerosol impacts on precipitation occurrence in warm maritime clouds. *J. Geophys. Res.*, **114**, D09211, <https://doi.org/10.1029/2008JD011273>.
- Lebsack, M. D., 2011: Level 2C RAIN-PROFILE product process description and interface control document, algorithm version 0.0. CloudSat Data Processing Center, 114 pp., http://www.cloudsat.cira.colostate.edu/sites/default/files/products/files/2C-RAIN-PROFILE-PDICD.P_R04.20110620.pdf.
- , and T. S. L'Ecuyer, 2011: The retrieval of warm rain from CloudSat. *J. Geophys. Res.*, **116**, D20209, <https://doi.org/10.1029/2011JD016076>.
- , G. L. Stephens, and C. Kummerow, 2008: Multisensor satellite observations of aerosol effects on warm clouds. *J. Geophys. Res.*, **113**, D15205, <https://doi.org/10.1029/2008JD009876>.
- Lenschow, D. H., and Coauthors, 1988: Dynamics and Chemistry of Marine Stratocumulus (DYCOMS) experiment. *Bull. Amer. Meteor. Soc.*, **69**, 1058–1067, [https://doi.org/10.1175/1520-0477\(1988\)069<1058:DACOMS>2.0.CO;2](https://doi.org/10.1175/1520-0477(1988)069<1058:DACOMS>2.0.CO;2).
- Liu, D., Q. Liu, and L. Zhou, 2015: Underestimation of oceanic warm cloud occurrences by the Cloud Profiling Radar aboard CloudSat. *J. Meteor. Res.*, **29**, 576–593, <https://doi.org/10.1007/s13351-015-5027-5>.
- Marchand, R., G. G. Mace, T. Ackerman, and G. Stephens, 2008: Hydrometeor detection using *Cloudsat*—An Earth-orbiting 94-GHz cloud radar. *J. Atmos. Oceanic Technol.*, **25**, 519–533, <https://doi.org/10.1175/2007JTECHA1006.1>.
- Marshall, J. S., and W. M. K. Palmer, 1948: The distribution of raindrops with size. *J. Meteor.*, **5**, 165–166, [https://doi.org/10.1175/1520-0469\(1948\)005<0165:TDORWS>2.0.CO;2](https://doi.org/10.1175/1520-0469(1948)005<0165:TDORWS>2.0.CO;2).
- Matrosov, S. Y., T. Uttal, and D. A. Hazen, 2004: Evaluation of radar reflectivity-based estimates of water content in stratiform marine clouds. *J. Appl. Meteor.*, **43**, 405–419, [https://doi.org/10.1175/1520-0450\(2004\)043<0405:EORREO>2.0.CO;2](https://doi.org/10.1175/1520-0450(2004)043<0405:EORREO>2.0.CO;2).
- Matus, A., T. S. L'Ecuyer, J. E. Kay, J.-F. Lamarque, and C. Hannay, 2015: The role of clouds in modulating global aerosol direct radiative effects in spaceborne active observations and the Community Earth System Model. *J. Climate*, **28**, 2986–3003, <https://doi.org/10.1175/JCLI-D-14-00426.1>.
- Meyer, K., S. Platnick, and Z. Zhang, 2015: Simultaneously inferring above-cloud absorbing aerosol optical thickness and underlying liquid phase cloud optical and microphysical properties using MODIS. *J. Geophys. Res. Atos.*, **120**, 5524–5547, <https://doi.org/10.1002/2015JD023128>.
- Mitrescu, C., S. D. Miller, J. M. Haynes, T. L'Ecuyer, and F. J. Turk, 2010: *CloudSat* Precipitation Profiling Algorithm—Model description. *J. Appl. Meteor. Climatol.*, **49**, 991–1003, <https://doi.org/10.1175/2009JAMC2181.1>.
- Mohrmann, J., R. Wood, J. McGibbon, R. Eastman, and E. Luke, 2018: Drivers of seasonal variability in marine boundary layer aerosol number concentration investigated using a steady state approach. *J. Geophys. Res. Atmos.*, **123**, 1097–1112, <https://doi.org/10.1002/2017JD027443>.
- Peers, F., and Coauthors, 2016: Comparison of aerosol optical properties above clouds between POLDER and AeroCom models over the South East Atlantic Ocean during the fire season. *Geophys. Res. Lett.*, **43**, 3991–4000, <https://doi.org/10.1002/2016GL068222>.
- Rauber, R. M., and Coauthors, 2007: Rain in Shallow Cumulus over the Ocean: The RICO campaign. *Bull. Amer. Meteor. Soc.*, **88**, 1912–1928, <https://doi.org/10.1175/BAMS-88-12-1912>.
- Salio, P., M. P. Hobouchian, Y. G. Skabar, and D. Vila, 2015: Evaluation of high-resolution satellite precipitation estimates over southern South America using a dense rain gauge network. *Atmos. Res.*, **163**, 146–161, <https://doi.org/10.1016/j.atmosres.2014.11.017>.

- Sayer, A. M., N. C. Hsu, C. Bettenhausen, J. Lee, J. Redemann, B. Schmid, and Y. Shinozuka, 2016: Extending “Deep Blue” aerosol retrieval coverage to cases of absorbing aerosols above clouds: Sensitivity analysis and first case studies. *J. Geophys. Res. Atmos.*, **121**, 4830–4854, <https://doi.org/10.1002/2015JD024729>.
- Sorooshian, A., G. Feingold, M. D. Lebsack, H. Jiang, and G. L. Stephens, 2009: On the precipitation susceptibility of clouds to aerosol perturbations. *Geophys. Res. Lett.*, **36**, L13803, <https://doi.org/10.1029/2009GL038993>.
- Stenz, R., X. Dong, B. Xi, Z. Feng, and R. J. Kuligowski, 2016: Improving satellite quantitative precipitation estimation using GOES-retrieved cloud optical depth. *J. Hydrometeor.*, **17**, 557–570, <https://doi.org/10.1175/JHM-D-15-0057.1>.
- Stephens, G. L., and Coauthors, 2010: Dreary state of precipitation in global models. *J. Geophys. Res.*, **115**, D24211, <https://doi.org/10.1029/2010JD014532>.
- Stevens, B., and G. Feingold, 2009: Untangling aerosol effects on clouds and precipitation in a buffered system. *Nature*, **461**, 607, <https://doi.org/10.1038/nature08281>.
- , W. R. Cotton, G. Feingold, and C. Moeng, 1998: Large-eddy simulations of strongly precipitating, shallow, stratocumulus-topped boundary layers. *J. Atmos. Sci.*, **55**, 3616–3638, [https://doi.org/10.1175/1520-0469\(1998\)055<3616:LESOSP>2.0.CO;2](https://doi.org/10.1175/1520-0469(1998)055<3616:LESOSP>2.0.CO;2).
- , and Coauthors, 2003: Dynamics and Chemistry of Marine Stratocumulus—DYCOMS-II. *Bull. Amer. Meteor. Soc.*, **84**, 579–594, <https://doi.org/10.1175/BAMS-84-5-579>.
- Tanelli, S., S. L. Durden, E. Im, K. S. Pak, D. G. Reinke, P. Partain, J. M. Haynes, and R. T. Marchand, 2008: CloudSat’s cloud profiling radar after two years in orbit: Performance, calibration, and processing. *IEEE Trans. Geosci. Remote Sens.*, **46**, 3560–3573, <https://doi.org/10.1109/TGRS.2008.2002030>.
- Trenberth, K. E., 2011: Changes in precipitation with climate change. *Climate Res.*, **47** (1–2), 123–138, <https://doi.org/10.3354/cr00953>.
- vanZanten, M. C., and Coauthors, 2011: Controls on precipitation and cloudiness in simulations of trade-wind cumulus as observed during RICO. *J. Adv. Model. Earth Syst.*, **3**, M06001, <https://doi.org/10.1029/2011MS000056>.
- Wang, H., G. Feingold, R. Wood, and J. Kazil, 2010: Modelling microphysical and meteorological controls on precipitation and cloud cellular structures in southeast Pacific stratocumulus. *Atmos. Chem. Phys.*, **10**, 6347–6362, <https://doi.org/10.5194/acp-10-6347-2010>.
- Warren, S. G., R. M. Eastman, and C. J. Hahn, 2007: A survey of changes in cloud cover and cloud types over land from surface observations, 1971–96. *J. Climate*, **20**, 717–738, <https://doi.org/10.1175/JCLI4031.1>.
- Wood, R., 2006: Rate of loss of cloud droplets by coalescence in warm clouds. *J. Geophys. Res.*, **111**, D21205, <https://doi.org/10.1029/2006JD007553>.
- , 2012: Stratocumulus clouds. *Mon. Wea. Rev.*, **140**, 2373–2423, <https://doi.org/10.1175/MWR-D-11-00121.1>.
- , and C. S. Bretherton, 2006: On the relationship between stratiform low cloud cover and lower-tropospheric stability. *J. Climate*, **19**, 6425–6432, <https://doi.org/10.1175/JCLI3988.1>.
- , —, and D. L. Hartmann, 2002: Diurnal cycle of liquid water path over the subtropical and tropical oceans. *Geophys. Res. Lett.*, **29**, 2092, <https://doi.org/10.1029/2002GL015371>.
- , and Coauthors, 2011: The VAMOS Ocean-Cloud-Atmosphere-Land Study Regional Experiment (VOCALS-REx): Goals, platforms, and field operations. *Atmos. Chem. Phys.*, **11**, 627–654, <https://doi.org/10.5194/acp-11-627-2011>.
- , and Coauthors, 2015: Clouds, aerosols, and precipitation in the marine boundary layer: An ARM Mobile Facility deployment. *Bull. Amer. Meteor. Soc.*, **96**, 419–440, <https://doi.org/10.1175/BAMS-D-13-00180.1>.
- , and Coauthors, 2018: Ultraclean layers and optically thin clouds in the stratocumulus-to-cumulus transition. Part I: Observations. *J. Atmos. Sci.*, **75**, 1631–1652, <https://doi.org/10.1175/JAS-D-17-0213.1>.
- Xue, H., G. Feingold, and B. Stevens, 2008: Aerosol effects on clouds, precipitation, and the organization of shallow cumulus convection. *J. Atmos. Sci.*, **65**, 392–406, <https://doi.org/10.1175/2007JAS2428.1>.
- Yamaguchi, T., G. Feingold, J. Kazil, and A. McComiskey, 2015: Stratocumulus to cumulus transition in the presence of elevated smoke layers. *Geophys. Res. Lett.*, **42**, 10 478–10 485, <https://doi.org/10.1002/2015GL066544>.
- Zhang, L., D. V. Michelangeli, and P. A. Taylor, 2004: Numerical studies of aerosol scavenging by low-level, warm stratiform clouds and precipitation. *Atmos. Environ.*, **38**, 4653–4665, <https://doi.org/10.1016/j.atmosenv.2004.05.042>.
- Zuidema, P., J. Redemann, J. Haywood, R. Wood, S. Piketh, M. Hipondoka, and P. Formenti, 2016: Smoke and clouds above the southeast Atlantic: Upcoming field campaigns probe absorbing aerosol’s impact on climate. *Bull. Amer. Meteor. Soc.*, **97**, 1131–1135, <https://doi.org/10.1175/BAMS-D-15-00082.1>.